Author's Accepted Manuscript

www.elsevier.com/locate/talanta

Particle Detection on Microfluidic Chips by Differential Resistive Pulse Sensing (RPS) Method

Ran Peng, Dongqing Li

PII: S0039-9140(18)30261-3
DOI: https://doi.org/10.1016/j.talanta.2018.03.023
Reference: TAL18457

To appear in: *Talanta*

Received date: 6 February 2018
Revised date: 5 March 2018
Accepted date: 9 March 2018

Cite this article as: Ran Peng and Dongqing Li, Particle Detection on Microfluidic Chips by Differential Resistive Pulse Sensing (RPS) Method, *Talanta,* https://doi.org/10.1016/j.talanta.2018.03.023

Particle Detection on Microfluidic Chips by Differential Resistive Pulse Sensing (RPS) Method

Ran Peng, Dongqing Li*

Department of Mechanical and Mechatronics Engineering, University of Waterloo, Waterloo, Ontario, Canada N2L 3G1

*Corresponding author, Email: dongqing@uwaterloo.ca

Abstract:

The resistive pulse sensing (RPS) method has been widely used for characterization of particles, cells, and biomolecules due to its merits of high sensitivity and resolution. This paper investigates working parameters involved in detecting submicron and micron-sized particles by the differential RPS method on microfluidic chips. Effects of particle-to-sensor size ratio, ionic concentration and pH of the electrolyte solution, and applied electric field are studied systematically by using polystyrene particles with a size range from 140 nm to 5 μm. The results show that both the amplitude and the signal-to-noise ratio (SNR) of the RPS signals increase with the particle-to-sensor size ratio as well as the ionic concentration of the electrolyte media. The amplitude of the RPS signals also increases with increasing applied voltage, while the SNR

experiences an upslope at low voltages and a decline under the condition of high voltages. pH has little effect on the background noise of the differential RPS signals but reduces the amplitude of the RPS signals at high pH. Grouping of RPS signals is considered to be caused by interactions between the sensor walls and the particles. Nanoparticle detection by the differential RPS method can be enhanced by optimizing these working parameters.

Keywords: Resistive Pulse Sensing (RPS); Nanoparticle Detection; Signal-to-Noise Ratio; Working Parameter Optimization

1. Introduction

Resistive pulse sensing technique has generated considerable interest as a powerful tool in chemical and biological fields due to its simple design and high sensitivity in detecting and sizing micro- and nano-particles. A lot of applications have been developed based on the RPS technique. For instance, detection and sequencing of individual DNA molecules based on the RPS technique have been reported recently [1–9]. Colloidal objects such as liposomes [10–12], oil droplets [13], nanoparticles [14–16], proteins [17–21], viruses [22–25], cells [26], bacteria [27] even individual organic molecules and ions [28–30] can also be detected by the RPS method. From RPS signals one can predict the size and concentration of particles, the shape of particles [10] as well as the shape of RPS sensors [31], and the surface charge and zeta potential of the detected objects [32–34]. Additionally, in comparison with other detection strategies, such as optical methods [35], the RPS method is label-free and compatible with the established nanofabrication techniques, consequently, the RPS method can be integrated with nanofluidic

systems and provides cost-effective and robust lab-on-a-chip applications [36]. However, to fully explore the potential of the RPS technique in practical applications, it is crucial to obtain high-quality RPS signals.

A traditional design of an RPS detection system for nano-sized objects is simply bridging two tanks of electrolyte solution with a nanopore or a nano-orifice [23,37–39]. An electric field is applied to build up a constant electric current through the nanopore. As a non-conducting particle passes through the nanopore and partially displaces the electrolyte, the stable electric current inside the nanopore is disturbed due to the conductivity change, generating a "pulse" signal which can be recorded by an ammeter. Theoretically, for a traditional RPS system, the amplitude of the RPS signal is proportional to the particle-to-pore size ratio, the applied voltage as well as the conductivity of the electrolyte solution [40,41]. To detect recognizable RPS signals, one has to investigate the effects of the parameters involved in the RPS measurements and to improve the signal-to-noise ratio (SNR). The noises can be categorized into two groups. The low-frequency noises come from the external electric power source, fluctuations of particles around the RPS sensor, collisions between particles and sensor walls, free charge carriers and the existence of nano-bubbles, and so on. The high-frequency components of the noises are due to the intrinsic properties of the electronic circuit [42,43]. To improve the SNR and to get rid of the limitations of the traditional RPS method, considerable efforts have been made. For instance, metal oxide semiconductor field effect transistor-based RPS devices have been developed by Xu et al., which enables detection of particle-to-pore size ratio down to 0.006% [44,45]. Later on, Wu et al. [43] developed a microfluidic-based differential RPS device by using a two-stage differential amplification method. The symmetric differential detecting channels are able to reduce the background noises efficiently, and a minimum detectable particle-to-pore volume

ratio of 0.0004% was achieved [43], showing potential capabilities in submicron and nano-sized particle sizing and detection.

As a promising characterization tool in nanoscience and nanotechnology, the differential RPS method has several merits over the traditional design. Combining nanofluidic and Lab-on-a-Chip technologies, the differential RPS system can be integrated onto a tiny piece of nanofluidic chip, which minimizes the bulky system of the traditional design on one hand and lowers the consumption of samples to picoliter level on the other hand. Moreover, differential RPS devices developed on PDMS platforms are reproducible, cost-effective, productive, which avoids tricky problems in fabricating traditional RPS systems, for example, complicated fabrication processes in making glass nanopipettes [23,37–39], high expenditure in fabricating solid-state nanopores by using standard techniques in the semiconductor industry [24,46], low repeatability and productivity by using unconventional materials such as carbon nanotubes (CNTs) [47–51] and tunable polymer nanopores [13,32,52,53]. In the differential RPS design, fluidic channels filled with conducting solutions are working as electrodes for differential signal acquisition, consequently, no fine printed electrodes are needed [54]. In addition, RPS systems made of PDMS have a relatively low background noise in comparison with those made of solid-state materials [15]. Based on the differential RPS design, a series of applications have been developed, for example, counting nanoparticles [55] and bacteria [27] on microfluidic chips. Recently, Peng and Li [14] reported a differential RPS system developed on a PDMS nanofluidic chip, demonstrating that nanoparticles of 23 nm in diameter and dsDNA molecules can be detected. The nanofluidic chip is simply composed of a microchannel-nanochannel structure, in which the nanochannel section works as the differential RPS sensor. The authors also demonstrated that the RPS system is capable of distinguishing 60 nm and 80 nm nanoparticles

and detecting folding and knotting of DNA chains. However, to fully utilize the advantages of the differential RPS technique developed on these kinds of nanofluidic chips and to improve the sensitivity and SNR in nano-sized or submicron-sized objects detection, a systematic study is needed to fully understand the working parameters involved in the detection.

In this paper, working parameters in detecting submicron-sized particles by the differential RPS method on microfluidic chips are studied systematically. Particle-to-pore size ratio effects are investigated by detecting polystyrene particles of different size ranging from 83 nm to 1 μm through one RPS sensor. KCl solutions ranging from 0.1 mM to 2 M are applied in detecting 140 nm, 500 nm and 5 μm particles to study the ionic concentration effects. Influences of pH value of the electrolyte and the applied electric field on the SNR in particle detection are also investigated. Particle loading frequency effects and particle loading trajectory effects on the channel-based differential RPS method are discussed. Conclusions on optimizing working parameters for detecting nanoparticles by the differential RPS method based on the experimental results are presented.

2. Material and methods

2.1 Working principle of differential RPS

Figure 1 (a) illustrates the working principle of the differential RPS system. The upstream and downstream sections of the main channel are connected by a submicron channel, and the system is powered by a DC electric field. Two symmetric microchannels located adjacent to the RPS gate work as the electrodes for differential signal acquisition. Figure 1 (b) is an equivalent electrical circuit of the detection system, where R_1 and R_3 are the electrical resistances of the upstream and the downstream of the main channel filled with electrolyte solution, and R_2 and ΔR are the electrical resistances of the RPS gate and the resistance change of the RPS sensor due to passing through of particles. R_a and R_d are the electrical resistances of the amplifier circuits and

the detecting channel. Considering a small particle size case ($d/D<0.5$) [56], the output of the RPS signals can be derived accordingly (see Eq. S13 of the Supplementary Information (SI) for the detail), where d and D are the diameters of the particle and the RPS gate, respectively. However, in this study, experimental data are not correlated to the mathematical model quantitatively due to the complexity and practicability of the equations. For practical applications of an RPS sizing system, a numerical fitting curve is commonly used.

Figure 2 shows a sketch of the RPS detection system developed in this study. A differential RPS chip with microchannels connected by a submicron channel is fabricated on a PDMS platform. DC power is applied to the upstream and downstream of the main channel through two reservoirs. Electrical pulse signals generated by the particles are detected by the two differential detecting channels through Pt electrodes and transferred to the differential amplifier. A data acquisition card and a self-compiled LabVIEW program are applied to collect the amplified signals. To minimize noises from the surroundings, shielding cables and a shielding box were applied during the experiments.

2.2 Fabrication of PDMS RPS nanofluidic chips

The microfluidic chip used in this study is composed of two layers of PDMS slabs, as shown in Figure 3(a). The PDMS microchannel system on the top layer was replicated by soft lithography method from a microchannel mold, and the microchannel mold was made by the standard photolithography method (SU8 photoresist, MicroChem). The microchannel system is about 5μm in depth, and there is a 6.4 μm long gap between the upstream and downstream of the main channel, which is bridged by a submicron channel on the bottom layer. The main channel on the top layer is 100 μm wide and 0.8 cm long, while the detecting channels are around 0.7 cm in length and 50 μm in width. The PDMS submicron channel on the bottom layer was replicated from a channel mold fabricated by an unconventional method. In this method, a solvent-induced

nanocrack on a polystyrene surface [57] was replicated on a photoresist layer by the nanoimprint technique [58]. More details and guidelines for making submicron channel molds can be found in the references [57,58]. The microchannels and the submicron-sized channels were duplicated onto PDMS surfaces by casting pre-curing PDMS (Sylgard 184, base to curing agent 10:1) onto the channel molds followed by a curing process at 80℃ for 2 hours. After peeling off, the microchannel system and the submicron channel on both PDMS slabs were treated with plasma for 60 s (Harrick plasma®, PDC-32G), and an alignment system [58] was used to bond these PDMS slabs together. Figure 3 (a) shows the working procedures in detail. To be noted, regular PDMS is soft, and small PDMS channels are likely to collapse after bonding; as a result, a thin layer of x-PDMS [58] (about 15 μm) was coated onto the channel molds and cured at 70℃ for 1 hour before casting of the above-mentioned regular PDMS. It should be noted that PDMS material could degrade in extreme environments, such as extreme high pH values, due to hygroscopic and hydrolytic degradation [59]. However, these effects only become appreciable at very long exposure time and extreme pH values. In this study, the PDMS chips were used for only once, and the working life of each chip was generally shorter that 30 mins. As a result, the effects of hygroscopicity of the PDMS material on the RPS detection were not considered in this study.

Figure 3 (b) and Figure 3 (c) show an example of the microfluidic chip after bonding and a zoomed-in view of the RPS sensing area, respectively. The size of submicron channels used in this study was measured by an AFM (Multimode™SPM, Digital Instruments) at five locations and average values are presented in this article. It should be noted that PDMS channels replicated from one positive channel mold have the same size, as a result, the size of PDMS channels replicated from one certain channel mold was measured for only once on one PDMS channel.

Figure 3 (d) and Figure 3 (e) illustrate an example of a submicron channel replicated on a PDMS surface and a cross-section of this channel. In this work, three chips with three different RPS gates were developed. The RPS gate of 2.4 μm in width and 2.5 μm in depth was used to study the particle-to-sensor volume ratio effects by detecting 1 μm, 500 nm, 220 nm, 140 nm, and 83 nm particles. The RPS gate of 455 nm in width and 430 nm in depth was used to investigate the ionic concentration effects, the pH effects and the applied voltage effects by detecting 140 nm nanoparticles. As a comparison work, a 16 μm wide and 15 μm deep micron-sized RPS gate was used to detect 5 μm particles.

2.3 Chemical reagents

KCl solutions ranging from 0.1 mM to 2 M were prepared by dissolving KCl (Fisher Scientific) into pure water (Mini Q, Direct-Q3, 18.2 MΩ·cm, pH 6.5). Triton X-100 (0.1% (v/v)) was applied in all the solutions to avoid aggregation of nanoparticles. Acidic and alkaline solutions (0.5 M HCl and 0.5 M KOH) were used to adjust the pH value of the KCl solutions. Particles of 5 μm (PS05N) 1 μm (PS04N), 500 nm (PS02N) and 220 nm (FC02F) in diameter were bought from Bangs Laboratories (10% solids, w/v), and polystyrene particles of 140 nm (G140) and 83 nm (G85B) in diameter were purchased from Thermo Fisher Scientific (1% solids, w/v). Before each testing, the particles were diluted in a specific electrolyte solution by 1000 times. The sample solutions were initially dispersed by using a vortex mixer for 30 s and further mixed by using an ultrasonic mixer (Fisher Scientific) for at least 2 minutes. For each electrolyte solution, the conductivity and the pH value were measured for at least 3 times (Omega PHH-128). During the experiments, the DC power (AJC Brand® Battery) was applied on the nanofluidic chip through Pt electrodes (Sigma-Aldrich), and the amplification factor of the single stage differential amplifier (AD620, Digi-Key) was 500. The signals were recorded by the data

acquisition card (USB 6259) working at 1 kHz sampling frequency. The sizes of the 1 μm, 500 nm, 220 nm and 140 nm particles were also measured by dynamic laser scattering (DLS) (Zetasizer Nano ZS90, Malvern).

2.4 Experimental procedures and data processing

The PDMS chip was initially filled with one kind of pure KCl electrolyte solution for 15 minutes prior to loading the particle samples. Afterward, Pt electrodes were inserted into the channel reservoirs, and a DC power was applied to the electrodes. The RPS signals were detected by the differential detecting channels and amplified by 500 times then recorded by a self-complied LabVIEW program simultaneously. A low pass Bessel filter working at 30 Hz was applied to remove high-frequency noises from the original data. Example movies of detecting 140 nm and 1 μm particles by using the differential RPS systems can be found in the SI. It should be noted that 1 kHz sampling rate is sufficient for this study because the duration time of the RPS events for all the cases in this work was around 50~200 ms. Additionally, for each case, i.e., one kind of solution, one RPS gate size, and one applied voltage, at least three fresh chips were prepared and the experiments were conducted on these chips independently. Data obtained by using these chips were organized on one histogram. All the experiments were conducted at room temperature around 23℃.

During the data processing, moving average technique was applied to evaluate the baseline of the raw data as reported by Plesa and Dekker [60]. For each case, at least 50 RPS events were analyzed. It is hard to determine the starting point and the ending point of an RPS event due to the entrance effects. To avoid errors in evaluating dwelling time of the RPS events, FWHM (Full Width at Half Maximum) durations of the RPS signals were calculated, and the FWHM dwelling time is applied throughout this article. Average values and standard derivations of the amplitudes

of the RPS events are evaluated and presented in the following sections. In this article, working parameter effects on the signal-to-noise ratio (SNR) of the differential RPS method were investigated. The SNR was calculated by

$$\mathrm{SNR} = \Delta V_{\mathrm{output}}/\delta. \quad (1)$$

where the noise level (δ) of each case was obtained by calculating the standard deviation of 1000 data points without RPS events, and $\Delta V_{\mathrm{output}}$ is the average amplitude of the RPS signals (see the SI for the equation). In addition, as mentioned above, for each case, at least three chips were used. However, for each chip, the noise level varies due to the uncertainty in the chip bonding process and variability in surface charge of the PDMS channels, etc. An average noise level was obtained to evaluate the SNR. It should be noted that the widely accepted threshold is 3~5 times of the noise level. In this article, for most cases, thresholds of 3~20 times of the noise level were applied to identify RPS events. However, for only extreme cases, the SNRs were very low and a vlaue of 3 times of the noise level failed to identify RPS events, as a result, a minimum value of 1.5 times of the noise level was used to identify RPS events to obtain comprehensive trends of the data.

3. Results and discussion

3.1 Particle-to-sensor volume ratio

According to the classical theory, the magnitude of an RPS signal generated by a non-conducting particle is the same as the resistance change of the sensor, while the resistance change of the sensor is dominated by the particle-to-sensor volume ratio [61]. To study the particle-to-sensor volume ratio effects on particle detection by the differential RPS method, particles of 1 μm, 500 nm, 220 nm, 140 nm and 83 nm were diluted in 0.5 M KCl solution and detected by one RPS gate. The RPS gate is about 6.4 μm long, 2.4 μm wide and 2.5 μm deep.

The corresponding particle-to-sensor volume ratios (γ) are 0.012, $1.5\times 10^{-3}, 1.3\times 10^{-4}, 3.2\times 10^{-5}$ and 6.1×10^{-6}, respectively. For all the cases, a 6 V DC voltage was applied to the main channel during the experiments. The experimental results are illustrated in Figure 4. Figure 4 (a) demonstrates the number percentage distributions of the RPS signals detected by using this RPS chip under the above-mentioned conditions. For this specific sensing gate, 83 nm nanoparticles were too small to be detected. Figure 4 (b) illustrates the particle-to-sensor volume ratio effects on the amplitude and the SNR of the RPS signals by detecting 1 μm, 500 nm, 220 nm and 140 nm particles. Examples of RPS signals of 1 μm, 500 nm, 220 nm and 140 nm particles are demonstrated in Figure 4 (c)-(f), respectively.

From Figure 4 (a) one can see that the distributions of these RPS magnitudes are well distinguished, showing superior resolution than that of the DLS method (see Figure S-1 of SI for the DLS data), which have also been verified and reported in the literature [14,62]. The average RPS amplitudes of the 1 μm, 500 nm, 220 nm and 140 nm particle cases are around 5 V, 0.5 V, 0.08 and 0.03 V, respectively, as shown in Figure 4 (b) (the red dashed line), and the corresponding spans of the bins are illustrated in Figure 4 (a). From Figure 4 (b) one can find that the relation between the amplitude of RPS signals and the particle-to-sensor volume ratio γ is not linear. According to the theory, when the particle is small in comparison with the pore diameter, the resistance change is a linear function of the particle volume [63], however, as the particle volume becomes large, the relationship between the electrical resistance change and the particle volume becomes increasingly nonlinear [40,41,64]. Similarly, the SNR of the RPS signals also increases with γ dramatically, as shown in Figure 4 (b), indicating that a larger size ratio γ gives rise to a higher SNR which is beneficial to the reliability of the particle detection. Examples of RPS signals of 1 μm, 500 nm, 220 nm and 140 nm particles are demonstrated in

Figure 4 (c)-(f). Apparently, both the amplitude and the SNR of the RPS events in Figure 4 (c) are much higher than that in Figure 4 (d), (e) and (f). RPS events detected under the condition of high γ are more recognizable than those of the low γ cases. For instance, one can see the RPS signals clearly in Figure 4 (c) but can hardly recognize the events in Figure 4 (e). As mentioned above, 83 nm nanoparticles were also detected by this chip under the same working condition, but the signals of the particles were immersed in the background noises due to the extremely low size ratio γ. Theoretically speaking, a large γ would improve the sensitivity and the SNR of the RPS detection efficiently, however, the upper limit is dependent on the sensor's physical size, because an extremely high γ may trigger problems in sample loading. As a result, a suitable γ is very important for nanoparticle detection by the differential RPS method.

3.2 Ionic concentration effects

Generally speaking, the RPS method works well with highly conductive electrolyte solutions and it is difficult to detect RPS events by using an electrolyte solution with an extremely low conductivity. The conductivity of an electrolyte solution is dominated by both the mobility and concentration of the mobile ions. In this section, KCl solutions ranging from 0.1 mM to 2 M were applied to detect both 140 nm and 5 μm particles by using two RPS gates of different size, 2.5 μm × 2.4 μm × 6.4 μm, and 16 μm × 15 μm × 20 μm, respectively. For the 140 nm particle cases, the particles were diluted in the above-mentioned KCl solutions, and a 1.5 V electric potential was applied along the main channel. For the 5 μm particle cases, a 9 V electric voltage was applied. It should be noted that in order to obtain reliable RPS signals, different electric fields were applied in the 140 nm cases and the 5 μm cases, and the electric field effects will be discussed in the following sections. Figure 5 shows the experimental results. Figure 5 (a) illustrates the distributions of the RPS amplitude of the 140 nm particles detected by using 0.01

M, 0.1 M, 0.5 M and 1 M KCl solutions, and the corresponding examples of RPS signals are presented in Figure 5 (b). The conductivity of the electrolyte solutions and the ionic concentration effects on the signal amplitude and the SNR of 140 nm and 5 μm particle cases are shown in Figure 5 (c) and Figure 5 (d), respectively.

From Figure 5 (a) and (b), one can see that both the amplitude and the SNR of the RPS signals increase with the ionic concentration. RPS events detected by using a high concentration solution, such as 1 M KCl, are more recognizable than that detected by utilizing a low concentration solution, 0.01 M KCl, for example, because the high conductivity of the high concentration solution. As shown in Figure 5 (c), the conductivity of the KCl solution increases with the ionic concentration dramatically, for instance, as the concentration increases from 0.1 mM to the 2 M, the conductivity increases from 0.15 mS/m to about 125 mS/m. The amplitudes of the RPS signals for both the 140 nm particles and the 5 μm particles follow the trend of the conductivity curve, which coincides with the model presented in Eq. (S13) of SI. The conductivity of electrolyte solution dominates the electrical resistance of the detecting channels R_d, which affects the input of the RPS signals (Eq. (S8) of the SI). From Eq. (S8), apparently, one can get a conclusion that a higher concentration electrolyte solution with a higher electric conductivity is beneficial for smaller particle detection by obtaining an RPS signal with larger amplitude. The conductivity effects on the magnitude of RPS signals was also verified by using other 5 kinds of electrolyte solutions (see Figure S-2 of the SI for the detail). From Figure S-2, one can also conclude that the amplitude of the RPS signals follows the trend of the conductivity.

Ionic concentration affects the SNR of the RPS detection by the same way. From Figure 5 (d), one can see that the SNR of the 140 nm cases increases with the ionic concentration

gradually from 7.6 to about 47 as the ionic concentration increases from 0.01 M to 1 M. For the 0.01 M case, it is difficult to identify the RPS events of the 140 nm particles due to the low SNR; however, for the 2 M case (not presented in the figure), 140 nm particles get aggregated in such a high ionic strength environment, consequently, it is also hard to detect reliable RPS events due to the blockage of the RPS gate. Examples of RPS signals of aggregated nanoparticles and blockage of the RPS gate due to high ionic concentration are demonstrated in Figure S-3 of SI. As a comparison case, the SNR of the 5 μm particle cases also increases with the ionic concentration in the range of 1 mM to 0.5 M, as shown in Figure 5 (d); however, the SNR decreases rapidly when the concentration increases further, while the amplitude of the RPS signals still increases with the ionic concentration (see Figure 5 (c)). One possible reason for the decrease of the SNR at high concentration is the electrolysis of water under the condition of high conductivity of the electrolyte and the high electric voltage applied along the main channel. Electrolysis of water will generate small air bubbles at the electrodes and change the pH value of the electrolyte solution, resulting in fluctuations of current in the main channel and giving rise to a higher level of background noise. The effects of the pH value and the applied voltage will be discussed in the following sections.

3.3 Applied voltage effects

The DC power applied to the main channel provides driven forces for the loading of particles through electrophoresis and electroosmosis on one hand and generates basic current and detectable signals on the other hand. However, the magnitude of the applied voltage affects the particle detection processes significantly. An electric voltage ranging from 1 V to 9 V was applied to investigate the electric field effects on detecting 140 nm particles by the differential RPS method. As comparison cases, 500 nm and 5 μm particles were also detected by using larger RPS gates. All the particles were diluted in 0.5 M KCl solution (pH4). Figure 6 shows the

experimental results in detail. Figure 6 (a) illustrates the distributions of the RPS amplitudes of 140 nm particles detected by applying 1 V, 1.5 V, 3 V, 6 V and 9 V electric voltages. From Figure 6 (a) one can see that the amplitude of the RPS signals increases with the applied voltage gradually. Figure 6 (b) and Figure 6 (c) illustrate the effects of the applied voltage on the amplitude and the SNR of the RPS signals for all these three particle cases.

In Figure 6 (b) one can see that the amplitudes of the RPS signals are almost linear with the applied voltage for all three particle cases, which coincides with the model derived in Eq. (S13) of the SI, where the output of the RPS amplitude is proportional to the applied electric voltage when the other parameters are identical, i. e., the same electrolyte solution, and the same particle-to-sensor volume ratio. Consequently, to obtain RPS signals with larger amplitudes, a higher applied voltage is essential. However, a high SNR is more desirable for recognizable RPS signals. Figure 6 (c) shows the applied voltage effects on the SNR of the differential RPS detection. The SNRs of these three particle cases increase with the applied voltage at low voltages and then decrease after reaching critical values. For instance, the SNR of the 5 μm case increases from 27 to about 85 when the applied voltage increases from 1.5 V to 6 V; however, the SNR value decreases to about 70 as the voltage increases to 9 V. The 500 nm case shows a similar trend. For the 140 nm particle case, the SNR is about 3 at 1 V and increases gradually to around 18 at 3 V and then reduces to about 6 when the applied voltage increases to 9 V.

Apparently, the increment of the SNR at low voltages is due to the increasing RPS signal amplitude as shown in Figure 6 (b). However, when the applied voltage becomes higher, new phenomena occur and affect the SNR. As mentioned above, a high voltage is likely to trigger electrolysis of water which gives rise to generating of air bubbles and changing of pH value of the electrolyte media. These factors contribute to a higher level of background noise. In addition,

the moving speed of particles is higher under the condition of higher electric fields. Collisions between the particles and collisions between the particles and the channel walls will also give rise to a higher noise level. Moreover, when a high electric field is applied to a small RPS gate, vortices are likely to be generated at the entrance and the exit of the sensing gate due to polarization of ions, electroosmotic flow of the second kind, induced-charge effects and so on [65–70]. The vortices induce fluctuations of the electrical current in the main channel and result in a higher noise level during RPS detection, especially for nano-sized RPS gates. For example, the SNR of detecting 140 nm particles at 3 V is about 18, and this value decreases by two-thirds to around 6 as 9 V is applied. Consequently, to obtain RPS signals with large amplitudes and high SNRs, a suitable applied voltage is crucial. Many published papers have studied the applied voltage effects on the RPS detection, and the RPS amplitude also increases with the applied voltage [24,71], however, in these papers, the effects of applied voltage on the SNR of the RPS detection have not been investigated.

3.4 pH effects

It is widely accepted that pH affects the surface charge properties of solid surfaces, and the surface charges dominate electrokinetic transport behaviors in both microfluidic and nanofluidic systems. Also, particle samples are usually required to be suspended in a specific pH environment; however, to the best of our knowledge, the effects of the pH environment on small particle detection by the RPS method have seldom been studied. In this section, KCl solutions with various pH values were applied to study the pH effects on particle detection. Particles of 5 μm, 500 nm, and 140 nm were diluted in the solution, and 9 V, 6 V, and 3 V electric voltages were applied along the main channels in the three particle cases, respectively. Figure 7 illustrates the pH effects on the particle detection in detail. Figure 7 (a) describes the conductivity of KCl solutions with pH values ranging from 1 to 13 and the amplitudes of RPS signals of 5 μm, 500

nm, and 140 nm particles detected by using these solutions. Figure 7 (b) gives the pH effects on the SNR of the RPS signals in detecting 140 nm particles, and Figure 7 (c) demonstrates the distribution of the RPS amplitude of the 140 nm particles. Examples of RPS signals recorded during detecting 140 nm particles by using pH 1, pH 4, pH 6 and pH 10 KCl solutions are demonstrated in Figure 7 (d).

From Figure 7 (a) one can see that the RPS amplitude for all three particle cases decreases with increasing pH sharply at low pH followed by a plateau in the middle and experiences a decreasing trend at high pH. The conductivity of the solutions decreases with increasing pH at low pH and arrives at a plateau in the mediate pH, however, increases again when the pH value is higher than 10, as shown in Figure 7 (a). The high conductivity at low and high pH values is due to the high ionic mobility of H^+ and OH^- ions [72]. It is obvious that the amplitudes of the RPS signals for all these three particle cases are dominated by the conductivity of the electrolyte media and follow the trend of the conductivity curve at low pH values. However, when the pH value becomes higher, the conductivity effects are less important, and the RPS amplitudes are mostly affected by the pH.

For instance, for the 140 nm particle cases, when the pH value increases from 1 to 2, the conductivity decreases from about 90 mS/m to around 53 mS/m while the signal amplitude decreases from 0.3 V to about 0.2 V. However, when the pH further increases from 6 to 12, the conductivity also increases from 47 mS/m to 55 mS/m, but the amplitude of the RPS signals decreases from about 0.2 V to 0.1 V. The trend of the SNR in Figure 7 (b) is almost identical with the signal amplitude curve in Figure 7 (a). However, the calculated background noise levels for all the cases are of the same magnitude, about 0.02 V. As a result, one can conclude that pH has little effect on the background noise but affects the amplitude of the RPS signals at high pH,

as intuitively shown in Figure 7 (d). From Figure 7 (d) one can see that RPS signals detected by using pH 1 solution are more recognizable than those by using higher pH solutions. On the other hand, from Figure 7 (a) one can see that the decrease of the RPS amplitude at high pH is more evident in the 140 nm particle case. One probable reason is that the charge effect on the RPS amplitude in the 140 nm particle case is more obvious than that in the 5 μm and 500 nm particle cases is that a small particle has a larger surface-to-volume ratio compared with large particles. Under the condition of high pH, small particles are highly negatively charged; as a result, the charges on the particles contribute partial conductivity to the RPS gate and reduce the amplitude of the RPS signals. While in the model presented in the SI, the particles are assumed to be perfectly non-conducting and pH has no effects on the amplitude of the RPS signals. However, in practical particle detection, to obtain RPS signals with large amplitudes and high SNRs, it is crucial to find a right electrolyte with a suitable pH value.

In addition, pH of the electrolyte solution plays an important role in sample loading and stabilization of particle suspensions in particle detection by affecting the surface charges of the RPS gate and the particles. In electrokinetic sample loading, the surface charges on the RPS gate and the particles combining with the externally applied electric field provide the driven forces for the fluid and the particles. However, at a specific pH value, sample loading by electroosmotic flow and electrophoresis may fail because the surface charges may become zero at this pH value, which is called PZC (point of zero charge) or isoelectric point. For example, during the experiments of this section, reversal of moving direction of the particles at a pH around 10 was observed. As a result, at pH 10, the velocity of the particles was very slow. Furthermore, the repulsion force between the entrance of the RPS gate and the particles stops the particles from entering the RPS gate, which is also a problem in particle loading in some circumstances. A

proper pH value can also stabilize the particle suspensions through enhancing the surface charges of the particles. To conclude, the pH of the electrolyte media affects the efficiency of electrokinetic sample loading, the duration time and amplitude of the RPS events, stability of the particle suspensions by dominating the surface charges of the RPS gates and the particles.

3.5 Particle concentration and loading trajectory effects

One can get the dynamic motion and the concentration of particles by evaluating the duration time and the frequency of the RPS signals, and for a channel-based RPS sensor, the dynamic motion of the particles is affected by the concentration and the trajectory of the particles. For example, when two successive particles are too close to each other, they will affect the motion of each other when passing through the RPS gate due to the electrostatic repulsion force between them. In addition, simultaneous translocation of two or more particles will generate larger RPS signals in comparison with those of single particle cases. The loading trajectory of particles also affects the shape of RPS signals. For example, off-axis translocations of particles may generate larger RPS signals compared with those of the on-axis cases [52,56,73] due to the non-uniform electric field inside the RPS gate. RPS signals are induced even before the entry of the particles [52,74,75]. As a result, attention should be paid to the trajectories of the particles during RPS detection.

Figure 8 demonstrates an example of grouping of RPS signals due to off-axis particle loading and interactions between the channel walls and the particles. In this case, 500 nm particles were diluted in 0.5 M KCl solution (pH 2) by 500 times and detected by applying 9 V along the main channel. To be noted, the trajectory effects may happen at any circumstance and the working condition demonstrated in part is just an example. Figure 8 (a) is a scatter diagram of the RPS signals. From Figure 8 (a) one can see that the signals are separated into two apparent groups. The amplitudes of the two groups of RPS signals are similar, as shown in Figure 8 (b), however,

the signals are separated into two groups by different durations (Figure 8 (c)). Figure 8 (d) is a zoomed-in view of the first-group RPS signals and the distributions of the amplitude and the duration time of these signals. A similar example of grouping of RPS signals detected by the differential RPS method is demonstrated in Figure S-4 of the SI.

Grouping of RPS signals by amplitude has been reported previously [52], and a variation in amplitude ranging from 10% ~ 35% has been presented [56,73]. However, in Figure 8 (a), the difference in the amplitude of these two groups of events is not so obvious, and the events are mainly grouped by duration time. The discrepancy in the grouping style is considered to be caused by the shape of the RPS gate and the interactions between the particles and the RPS gate. In the channel-based RPS detection, the RPS gate is a long channel and the electric field inside the channel is relatively uniform, as a result, off-axis translocations of particles will not contribute large amplitude changes in the RPS detection. However, as the particle size is comparable to the diameter of the RPS gate, off-axis particles are likely to touch the RPS gate walls and interact with the channel walls, resulting in a low transport speed and a long duration time. On the contrary, particles loaded along the central axis will pass through the RPS gate smoothly without any interactions, and the speed is high while the duration time is short. Consequently, the events of the translocations are divided into two apparent groups, one group with shorter duration time and without channel wall-particle interactions and one group with longer duration time due to the interactions between the channel walls and the particles, as shown in Figure 8 (a). Consequently, one may predict that for long channel-based RPS gates, the grouping behavior is dominated by the particle-wall interactions, and the RPS events are mainly grouped by duration time, for example, more than 50% in difference as illustrated in Figure 8(a).

A video demonstrating the off-axis effect in RPS detection recorded during the experiments can be found in the SI.

It is impossible to avoid the circumstance of simultaneous loading of particles theoretically. Entering of two particles into the RPS gate at once will generate a larger RPS signal compared with that of a single particle case. An example of simultaneous transport of particles is demonstrated in Figure S-3 of the SI. However, the possibility of the simultaneous loading situation can be minimized by controlling the concentration of the particle samples. In theory, the highest particle concentration (volume ratio v/v) that an RPS system can handle in a one-by-one detection style is the same as that of the particle-to-sensor volume ratio (γ). In the experiments, the particle samples are usually diluted to make sure the one-by-one detection process.

4. Conclusions

This paper investigates key working parameters in the differential RPS method in submicron particle detection by experiments. The effects of particle-to-sensor size ratio, ionic concentration and pH of the electrolyte solution, applied voltage, as well as the particle loading trajectory on the differential RPS method are studied. The results show that both the amplitude and the SNR of the RPS signals increase with the particle-to-sensor size ratio and the conductivity of the electrolyte media. The amplitude of RPS signals also increases with the applied voltage. However, the SNR increases with the applied voltage only when the voltage is lower than a critical value, and when the applied voltage is higher than the critical value, the SNR decreases with the voltage gradually. pH has little effect on the background noise of the differential RPS detection but reduces the amplitude of the RPS signals at high pH. RPS events could be divided into groups due to the off-axis effect and interactions between the channel walls and the particles. Aggregation of small particles under the condition of extremely high ionic strength, extremely low pH, instability of electric current through the RPS gate at a high driven electric

field would lower the effectiveness of the differential RPS method. The present study provides a framework for the applications of the differential RPS method in particle detection. Detection of nanoparticles by the differential RPS method can be enhanced by optimizing these working parameters. In addition, based on the systematic study presented in this paper, the device also offers potential applications in the fundamental research areas such as microfluidics, nanofluidics as well as interfacial sciences by analyzing the shape, amplitude, duration of the RPS signals. The potential applications may include investigating electrokinetic transport of particles in a confined space, detecting surface charge of particles, capturing and manipulating of particles, and detecting deformation of targets.

Acknowledgment

The authors wish to thank the financial support of the Natural Sciences and Engineering Research Council (NSERC) of Canada through a research grant to D. Li.

Notes

The authors declare no competing financial interest.

Video Caption

Video 1: Detection of 1um particles by the differential RPS method

Video 2: Detection of 140 nm particles by the differential RPS method

Video 3: An example of trajectory effect on RPS detection

References

[1] L.J. Steinbock, O. Otto, C. Chimerel, J. Gornall, U.F. Keyser, Detecting DNA folding

with nanocapillaries, Nano Lett. 10 (2010) 2493–2497. doi:10.1021/nl100997s.

[2] P. Waduge, R. Hu, P. Bandarkar, H. Yamazaki, B. Cressiot, Q. Zhao, P.C. Whitford, M. Wanunu, Nanopore-Based Measurements of Protein Size, Fluctuations, and Conformational Changes, ACS Nano. 11 (2017) 5706–5716. doi:10.1021/acsnano.7b01212.

[3] C. Plesa, D. Verschueren, S. Pud, J. van der Torre, J.W. Ruitenberg, M.J. Witteveen, M.P. Jonsson, A.Y. Grosberg, Y. Rabin, C. Dekker, Direct observation of DNA knots using a solid-state nanopore, Nat. Nanotechnol. 11 (2016) 1093–1097. doi:10.1038/nnano.2016.153.

[4] D. Kaya, A. Dinler, N. San, K. Kececi, Effect of Pore Geometry on Resistive-Pulse Sensing of DNA Using Track-Etched PET Nanopore Membrane, Electrochim. Acta. 202 (2016) 157–165. doi:10.1016/j.electacta.2016.04.014.

[5] J. Sha, T. Hasan, S. Milana, C. Bertulli, N.A.W. Bell, G. Privitera, Z. Ni, Y. Chen, F. Bonaccorso, A.C. Ferrari, U.F. Keyser, Y.Y.S. Huang, Nanotubes complexed with DNA and proteins for resistive-pulse sensing, ACS Nano. 7 (2013) 8857–8869. doi:10.1021/nn403323k.

[6] L.J. Steinbock, R.D. Bulushev, S. Krishnan, C. Raillon, A. Radenovic, DNA translocation through low-noise glass nanopores, ACS Nano. 7 (2013) 11255–11262. doi:10.1021/nn405029j.

[7] G.M. Cherf, K.R. Lieberman, H. Rashid, C.E. Lam, K. Karplus, M. Akeson, Automated forward and reverse ratcheting of DNA in a nanopore at 5-Å precision., Nat. Biotechnol. 30 (2012) 344–8. doi:10.1038/nbt.2147.

[8] L.D. Menard, C.E. Mair, M.E. Woodson, J.P. Alarie, J.M. Ramsey, A device for

performing lateral conductance measurements on individual double-stranded DNA molecules, ACS Nano. 6 (2012) 9087–9094. doi:10.1021/nn303322r.

[9] C. Raillon, P. Granjon, M. Graf, L.J. Steinbock, A. Radenovic, Fast and automatic processing of multi-level events in nanopore translocation experiments, Nanoscale. 4 (2012) 4916. doi:10.1039/c2nr30951c.

[10] A. Darvish, G. Goyal, R. Aneja, R.V. Kalyana Sundaram, K. Lee, C.W. Ahn, K.-B. Kim, P. Vlahovska, M.J. Kim, Nanoparticle mechanics: deformation detection via nanopore resistive pulse sensing, Nanoscale. 8 (2016) 14420–14431. doi:10.1039/C6NR03371G.

[11] D.A. Holden, J.J. Watkins, H.S. White, Resistive-pulse detection of multilamellar liposomes, Langmuir. 28 (2012) 7572–7577. doi:10.1021/la300993a.

[12] Y. Rudzevich, Y. Lin, A. Wearne, A. Ordonez, O. Lupan, L. Chow, Characterization of liposomes and silica nanoparticles using resistive pulse method, Colloids Surfaces A Physicochem. Eng. Asp. 448 (2014) 9–15. doi:10.1016/j.colsurfa.2014.01.080.

[13] J.A. Somerville, G.R. Willmott, J. Eldridge, M. Griffiths, K.M. McGrath, Size and charge characterisation of a submicrometre oil-in-water emulsion using resistive pulse sensing with tunable pores, J. Colloid Interface Sci. 394 (2013) 243–251. doi:10.1016/j.jcis.2012.11.071.

[14] R. Peng, D. Li, Detection and sizing of nanoparticles and DNA on PDMS nanofluidic chips based on differential resistive pulse sensing, Nanoscale. 9 (2017) 5964–5974. doi:10.1039/C7NR00488E.

[15] T. Ito, L. Sun, R.M. Crooks, Simultaneous determination of the size and surface charge of individual nanoparticles using a carbon nanotube-based coulter counter, Anal. Chem. 75 (2003) 2399–2406. doi:10.1021/ac023072v ER.

[16] S.R. German, T.S. Hurd, H.S. White, T.L. Mega, Sizing Individual Au Nanoparticles in Solution with Sub-Nanometer Resolution, ACS Nano. 9 (2015) 7186–7194. doi:10.1021/acsnano.5b01963.

[17] E.L.C.J. Blundell, L.J. Mayne, M. Lickorish, S.D.R. Christie, M. Platt, Protein detection using tunable pores: resistive pulses and current rectification, Faraday Discuss. 193 (2016) 487–505. doi:10.1039/C6FD00072J.

[18] J. Larkin, R.Y. Henley, M. Muthukumar, J.K. Rosenstein, M. Wanunu, High-bandwidth protein analysis using solid-state nanopores, Biophys. J. 106 (2014) 696–704. doi:10.1016/j.bpj.2013.12.025.

[19] W. Li, N.A.W. Bell, S. Hernández-Ainsa, V. V. Thacker, A.M. Thackray, R. Bujdoso, U.F. Keyser, Single protein molecule detection by glass nanopores, ACS Nano. 7 (2013) 4129–4134. doi:10.1021/nn4004567.

[20] R. Wei, V. Gatterdam, R. Wieneke, R. Tampé, U. Rant, Stochastic sensing of proteins with receptor-modified solid-state nanopores., Nat. Nanotechnol. 7 (2012) 257–63. doi:10.1038/nnano.2012.24.

[21] K.J. Freedman, M. Jurgens, A. Prabhu, C.W. Ahn, P. Jemth, J.B. Edel, M.J. Kim, Chemical, thermal, and electric field induced unfolding of single protein molecules studied using nanopores, Anal. Chem. 83 (2011) 5137–5144. doi:10.1021/ac2001725.

[22] K. Zhou, L. Li, Z. Tan, A. Zlotnick, S.C. Jacobson, Characterization of hepatitis B virus capsids by resistive-pulse sensing, J. Am. Chem. Soc. 133 (2011) 1618–1621. doi:10.1021/ja108228x.

[23] P. Terejánszky, I. Makra, P. Fürjes, R.E. Gyurcsányi, Calibration-less sizing and quantitation of polymeric nanoparticles and viruses with quartz nanopipets, Anal. Chem.

86 (2014) 4688–4697. doi:10.1021/ac500184z.

[24] Z.D. Harms, D.G. Haywood, A.R. Kneller, L. Selzer, A. Zlotnick, S.C. Jacobson, Single-particle electrophoresis in nanochannels, Anal. Chem. 87 (2015) 699–705. doi:10.1021/ac503527d.

[25] Z.D. Harms, K.B. Mogensen, P.S. Nunes, K. Zhou, B.W. Hildenbrand, I. Mitra, Z. Tan, A. Zlotnick, J.P. Kutter, S.C. Jacobson, Nanofluidic devices with two pores in series for resistive-pulse sensing of single virus capsids, Anal. Chem. 83 (2011) 9573–9578. doi:10.1021/ac202358t.

[26] Y. Song, R. Peng, J. Wang, X. Pan, Y. Sun, D. Li, Automatic particle detection and sorting in an electrokinetic microfluidic chip., Electrophoresis. 34 (2013) 684–90. doi:10.1002/elps.201200416.

[27] Y. Song, H. Zhang, C.H. Chon, S. Chen, X. Pan, D. Li, Counting bacteria on a microfluidic chip, Anal. Chim. Acta. 681 (2010) 82–86. doi:10.1016/j.aca.2010.09.035.

[28] J. Feng, K. Liu, M. Graf, D. Dumcenco, A. Kis, M. Di Ventra, A. Radenovic, Observation of ionic Coulomb blockade in nanopores, Nat. Mater. 15 (2016) 850–855. doi:10.1038/nmat4607.

[29] W. Song, P. Pang, J. He, S. Lindsay, Optical Detection of Single Molecule Translocation through Carbon Nanotubes, ACS Nano. 7 (2013) 689–694.

[30] F. Haque, J. Li, H.C. Wu, X.J. Liang, P. Guo, Solid-state and biological nanopore for real-time sensing of single chemical and sequencing of DNA, Nano Today. 8 (2013) 56–74. doi:10.1016/j.nantod.2012.12.008.

[31] M. Pevarnik, K. Healy, M.E. Toimil-Molares, A. Morrison, S.E. Létant, Z.S. Siwy, Polystyrene particles reveal pore substructure as they translocate, ACS Nano. 6 (2012)

7295–7302. doi:10.1021/nn302413u.

[32] D. Kozak, W. Anderson, R. Vogel, S. Chen, F. Antaw, M. Trau, Simultaneous size and zeta-potential measurements of individual nanoparticles in dispersion using size-tunable pore sensors, ACS Nano. 6 (2012) 6990–6997. doi:10.1021/nn3020322.

[33] N. Panday, G. Qian, X. Wang, S. Chang, P. Pandey, J. He, Simultaneous Ionic Current and Potential Detection of Nanoparticles by A Multifunctional Nanopipette, ACS Nano. 10 (2016) 11237–11248. doi:10.1021/acsnano.6b06307.

[34] N. Arjmandi, W. Van Roy, L. Lagae, G. Borghs, Measuring the Electric Charge and Zeta Potential of Nanometer-Sized Objects Using Pyramidal-Shaped Nanopores, Anal. Chem. 84 (2012) 8490–8496. doi:10.1021/ac300705z.

[35] G.G. Daaboul, C.A. Lopez, J. Chinnala, B.B. Goldberg, J.H. Connor, M. Selim Ünlü, Digital sensing and sizing of vesicular stomatitis virus pseudotypes in complex media: A model for ebola and marburg detection, ACS Nano. 8 (2014) 6047–6055. doi:10.1021/nn501312q.

[36] A. Yurt, G.G. Daaboul, J.H. Connor, B.B. Goldberg, M. Selim Ünlü, Single nanoparticle detectors for biological applications, Nanoscale. 4 (2012) 715. doi:10.1039/c2nr11562j.

[37] H. Cai, Y. Wang, Y. Yu, M. V. Mirkin, S. Bhakta, G.W. Bishop, A. a. Joshi, J.F. Rusling, Resistive-Pulse Measurements with Nanopipettes: Detection of Vascular Endothelial Growth Factor C (VEGF-C) Using Antibody-Decorated Nanoparticles, Anal. Chem. 87 (2015) 6403–6410. doi:10.1021/acs.analchem.5b01468.

[38] W.J. Lan, D.A. Holden, B. Zhang, H.S. White, Nanoparticle transport in conical-shaped nanopores, Anal. Chem. 83 (2011) 3840–3847. doi:10.1021/ac200312n.

[39] Y. Wang, K. Kececi, M. Mirkin, V. Mani, Resistive-pulse measurements with

nanopipettes: detection of Au nanoparticles and nanoparticle-bound anti-peanut IgY, Chem. Sci. 4 (2013) 655–663. doi:10.1039/C2SC21502K.

[40] R.W. DeBlois, C.P. Bean, R.K.A. Wesley, Electrokinetic measurements with submicron particles and pores by the resistive pulse technique, J. Colloid Interface Sci. 61 (1977) 323–335. doi:10.1016/0021-9797(77)90395-2.

[41] R.W. DeBlois, C.P. Bean, Counting and Sizing of Submicron Particles by the Resistive Pulse Technique, Rev. Sci. Instrum. 41 (1970) 909. doi:10.1063/1.1684724.

[42] R.M.M. Smeets, U.F. Keyser, N.H. Dekker, C. Dekker, Noise in solid-state nanopores, Proc. Natl. Acad. Sci. 105 (2008) 417–421. doi:10.1073/pnas.0705349105.

[43] X. Wu, Y. Kang, Y.N. Wang, D. Xu, D. Li, D. Li, Microfluidic differential resistive pulse sensors, Electrophoresis. 29 (2008) 2754–2759. doi:10.1002/elps.200700912.

[44] M. Sridhar, D. Xu, Y. Kang, A.B. Hmelo, L.C. Feldman, D. Li, D. Li, Experimental characterization of a metal-oxide-semiconductor field-effect transistor-based Coulter counter, J. Appl. Phys. 103 (2008). doi:10.1063/1.2931026.

[45] D. Xu, Y. Kang, M. Sridhar, A.B. Hmelo, L.C. Feldman, D. Li, D. Li, Wide-spectrum, ultrasensitive fluidic sensors with amplification from both fluidic circuits and metal oxide semiconductor field effect transistors, Appl. Phys. Lett. 91 (2007) 1–4. doi:10.1063/1.2753123.

[46] M. Davenport, K. Healy, M. Pevarnik, N. Teslich, S. Cabrini, A.P. Morrison, Z.S. Siwy, S.E. Létant, The role of pore geometry in single nanoparticle detection, ACS Nano. 6 (2012) 8366–8380. doi:10.1021/nn303126n.

[47] M.D. Ellison, S. Menges, L. Nebel, G. D'Arcangelo, A. Kramer, L. Drahushuk, J. Benck, S. Shimizu, M.S. Strano, Electrokinetic Transport of Methanol and Lithium Ions Through

a 2.25-nm-Diameter Carbon Nanotube Nanopore, J. Phys. Chem. C. 121 (2017) 2005–2013. doi:10.1021/acs.jpcc.6b12104.

[48] K.V. Agrawal, L.W. Drahushuk, M.S. Strano, Observation and analysis of the Coulter effect through carbon nanotube and graphene nanopores, Philos. Trans. R. Soc. A Math. Phys. Eng. Sci. 374 (2016) 20150357. doi:10.1098/rsta.2015.0357.

[49] J.H. Park, J. He, B. Gyarfas, S. Lindsay, P.S. Krstić, DNA translocating through a carbon nanotube can increase ionic current, Nanotechnology. 23 (2012) 455107. doi:10.1088/0957-4484/23/45/455107.

[50] H.H. Liu, J. He, J. Tang, P. Pang, D. Cao, P. Krstic, S. Joseph, S. Lindsay, C. Nuckolls, H.H. Liu, P. Pang, D. Cao, P. Krstic, S. Joseph, S. Lindsay, C. Nuckolls, Translocation of Single-Stranded DNA Through Single-Walled Carbon Nanotubes, Science. 327 (2010) 64–67. doi:10.1126/science.1181799.

[51] J. He, H. Liu, P. Pang, D. Cao, S. Lindsay, Translocation events in a single-walled carbon nanotube, J. Phys. Condens. Matter. 22 (2010) 454112. doi:10.1088/0953-8984/22/45/454112.

[52] E. Weatherall, P. Hauer, R. Vogel, G.R. Willmott, Pulse Size Distributions in Tunable Resistive Pulse Sensing, Anal. Chem. 88 (2016) 8648–8656. doi:10.1021/acs.analchem.6b01818.

[53] M. Platt, G.R. Willmott, G.U. Lee, Resistive pulse sensing of analyte-induced multicomponent rod aggregation using tunable pores, Small. 8 (2012) 2436–2444. doi:10.1002/smll.201200058.

[54] X. Liang, S.Y. Chou, Nanogap detector inside nanofluidic channel for fast real-time label-free DNA analysis, Nano Lett. 8 (2008) 1472–1476. doi:10.1021/nl080473k.

[55] Y. Song, H. Zhang, C.H. Chon, X. Pan, D. Li, Nanoparticle detection by microfluidic Resistive Pulse Sensor with a submicron sensing gate and dual detecting channels-two stage differential amplifier, Sensors Actuators, B Chem. 155 (2011) 930–936. doi:10.1016/j.snb.2011.01.004.

[56] Z. Qin, J. Zhe, G. Wang, Effects of particle's off-axis position, shape, orientation and entry position on resistance changes of micro Coulter counting devices, Meas. Sci. Technol. 22 (2011) 45804. doi:10.1088/0957-0233/22/4/045804.

[57] R. Peng, D. Li, Fabrication of nanochannels on polystyrene surface, Biomicrofluidics. 9 (2015) 24117. doi:10.1063/1.4918643.

[58] R. Peng, D. Li, Fabrication of polydimethylsiloxane (PDMS) nanofluidic chips with controllable channel size and spacing, Lab Chip. 16 (2016) 3767–3776. doi:10.1039/C6LC00867D.

[59] J.L. Goudie, M.J. Owen, D.C. Corporation, A Review of Possible Degradation Mechanisms of Silicone Elastomers in Voltage Insulation Applications, Electr. Insul. Dielectr. Phenomena, 1998. Annu. Report. Conf. , vol.1, No., pp.120,127 Vol. 1,. 1 (1998) 120–127. doi:10.1109/CEIDP.1998.733878.

[60] C. Plesa, C. Dekker, Data analysis methods for solid-state nanopores, Nanotechnology. 26 (2015) 84003. doi:10.1088/0957-4484/26/8/084003.

[61] D. Kozak, W. Anderson, R. Vogel, M. Trau, Advances in resistive pulse sensors: Devices bridging the void between molecular and microscopic detection, Nano Today. 6 (2011) 531–545. doi:10.1016/j.nantod.2011.08.012.

[62] W. Anderson, D. Kozak, V.A. Coleman, Å.K. Jämting, M. Trau, A comparative study of submicron particle sizing platforms: Accuracy, precision and resolution analysis of

polydisperse particle size distributions, J. Colloid Interface Sci. 405 (2013) 322–330. doi:10.1016/j.jcis.2013.02.030.

[63] Lord Rayleigh, On the influence of obstacles arranged in rectangular order upon the properties of a medium, Philos. Mag. Ser. 5. 34 (1892) 481–502. doi:10.1080/14786449208620364.

[64] E.C. Gregg, K.D. Steidley, Electrical Counting and Sizing of Mammalian Cells in Suspension, Biophys. J. 5 (1965) 393–405. doi:10.1016/S0006-3495(65)86724-8.

[65] Y. Green, S. Park, G. Yossifon, Bridging the gap between an isolated nanochannel and a communicating multipore heterogeneous membrane, Phys. Rev. E - Stat. Nonlinear, Soft Matter Phys. 91 (2015) 1–6. doi:10.1103/PhysRevE.91.011002.

[66] R.A. Prabhakaran, Y. Zhou, C. Zhao, G. Hu, Y. Song, J. Wang, C. Yang, X. Xuan, Induced charge effects on electrokinetic entry flow, Phys. Fluids. 29 (2017) 62001. doi:10.1063/1.4984741.

[67] I. Cho, G.Y. Sung, S.J. Kim, Overlimiting current through ion concentration polarization layer: hydrodynamic convection effects, Nanoscale. 6 (2014) 4620. doi:10.1039/c3nr04961b.

[68] G. Yossifon, H.C. Chang, Selection of nonequilibrium overlimiting currents: Universal depletion layer formation dynamics and vortex instability, Phys. Rev. Lett. 101 (2008) 1–4. doi:10.1103/PhysRevLett.101.254501.

[69] B. Zaltzman, I. Rubinstein, Electro-osmotic slip and electroconvective instability, J. Fluid Mech. 579 (2007) 173–266. doi:10.1017/S0022112007004880.

[70] E.V. Dydek, B. Zaltzman, I. Rubinstein, D.S. Deng, A. Mani, M.Z. Bazant, Overlimiting current in a microchannel, Phys. Rev. Lett. 107 (2011) 1–5.

doi:10.1103/PhysRevLett.107.118301.

[71] E.L.C.J. Blundell, R. Vogel, M. Platt, Particle-by-Particle Charge Analysis of DNA-Modified Nanoparticles Using Tunable Resistive Pulse Sensing, Langmuir. 32 (2016) 1082–1090. doi:10.1021/acs.langmuir.5b03024.

[72] J.H. Masliyah, S. Bhattacharjee, Electrokinetic and colloid transport phenomena, John Wiley & Sons, 2006.

[73] M. Tsutsui, Y. He, K. Yokota, A. Arima, S. Hongo, M. Taniguchi, T. Washio, T. Kawai, Particle trajectory-dependent ionic current blockade in low-aspect-ratio pores, ACS Nano. 10 (2016) 803–809. doi:10.1021/acsnano.5b05906.

[74] Y. Qiu, Z. Siwy, Probing Charges on Solid-Liquid Interfaces with the Resistive-Pulse Technique, Nanoscale. (2017) 13527–13537. doi:10.1039/C7NR03998K.

[75] J.E. Hall, Access resistance of a small circular pore, J. Gen. Physiol. 66 (1975) 531–532. doi:10.1085/jgp.66.4.531.

Figure 1. Schematics of working principle of a nanochannel-based differential RPS chip. (a) Layout and mechanism of the differential RPS chip design. The upstream and downstream of a micron-sized microchannel is connected by a submicron channel. The channels are filled with electrolyte solution. A DC electric field is applied along the main channel. Two detecting channels located at the two ends of the RPS gate work as the differential signal acquisition electrodes. (b) An equivalent electrical circuit of the differential RPS design. R_2 and ΔR are the electrical resistance of the RPS gate and the electrical resistance change caused by passing through of a particle. R_1 and R_3 are the electrical resistances of the upstream section and the

downstream section of the main channel. R_d and R_a are the electrical resistances of the detecting channels and the amplifier circuits.

Figure 2. A sketch of the differential RPS detection system. The microchannel is used for sample loading. A DC electric field is applied to the main channel to drive the particles. A differential amplification circuit connecting to a data acquisition card is used to collect signals of the particles and LabVIEW programs are used to control the RPS signal acquisition process.

Figure 3. Fabrication of differential RPS microfluidic chips for submicron particle detection. (a) Components of a PDMS microfluidic chip, with a microchannel system on the top layer a single sensing channel on the bottom layer. (b) An example of RPS chip after bonding. (c) A zoomed-in view of the RPS gate area. (d) A 3-D image of the sensing gate and (e) a cross-section of this sensing gate measured by AFM.

Figure 4. Particle-to-sensor volume ratio γ effects on particle detection by the differential RPS method. The RPS sensor was about 6.4 μm long, 2.4 μm wide and 2.5 μm deep, and the applied voltage was 6 V. Particles of 1 μm, 500 nm, 220 nm and 140 nm in diameter were dispersed in 0.5 M KCl solution. (a) Distributions RPS amplitudes of 1μm, 500 nm, 220 nm and 140 nm particles. (b) Volume ratio effects on the RPS signal amplitudes and SNRs. (c)-(f) Examples of RPS events of 1 μm, 500 nm, 220 nm and 140 nm particles detected by the RPS chip.

Figure 5. Ionic concentration effects on the amplitude and the SNR in particle detection by the differential RPS method. (a) Distributions of RPS amplitudes of 140 nm particles detected by using 0.01 M，0.1 M, 0.5 M, and 1 M KCl solutions. (b) Examples of RPS signals of 140 nm particles detected by using 0.01 M，0.1 M, 0.5 M and 1 M KCl solutions, respectively. (c) The conductivity of the solutions and ionic concentration effects on the RPS signal amplitudes of 140

nm and 5 μm particles. Error bars of the conductivity are too small in comparison with the symbols which are neglected in the figure. (d) Ionic concentration effects on the SNR in detecting 140 nm and 5 μm particles by the differential RPS method.

Figure 6. Applied voltage effects on detecting particles by the differential RPS method. (a) Distributions of the RPS amplitudes of 140 nm nanoparticles detected by applying 1 V, 1.5 V, 3 V, 6 V, 9 V electric voltages, respectively. (b) Applied voltage effects on the RPS amplitude in detecting 5 μm, 500 nm and 140 nm particles. (c) Applied voltage effects on the SNR in detecting 5μm, 500 nm and 140 nm particles. All the particles were diluted in 0.5 M KCl solution (pH4). Error bars smaller than the symbols (500 nm and 140 nm cases) are neglected.

Figure 7. pH effects on particle detection by the differential RPS method. The particles were diluted in 0.5 M KCl solution, and 9 V, 6 V and 3 V electric voltages were applied in the 5 μm, 500 nm and 140 nm particle cases, respectively. (a) Conductivity of 0.5 M KCl solutions with pH ranging from pH 1 to pH 13 and RPS amplitudes of 5 μm, 500 nm and, 140 nm particles detected by using these solutions. (b) pH effects on the SNR in detecting 140 nm particles. (c) Distributions of RPS amplitudes in 140 nm particle detection and (d) RPS signals of 140 nm particles detected by using pH 1, pH 4, pH 6 and pH 10 KCl solutions. The red lines indicate the noise level of each case.

Figure 8. An example of grouping RPS signals caused by off-axis particle loading. (a) Scatter diagram of RPS signals of 500 nm particles detected by the differential RPS. (b) Distribution of the RPS signal amplitude in (a). (c) Distribution of dwelling time of the RPS signals in (a). (d) A zoomed-in view of the first-group RPS signals.

Highlights

- Systematic study of detecting submicron particles by differential resistive pulse sensing (RPS) method.
- Buffer solution (concentration, pH value and conductivity) effects on the amplitude and signal-to-noise ratio (SNR) of RPS signals.
- Sample loading trajectory effects on the RPS detecting method.
- Improved understanding of differential RPS method in practical applications.

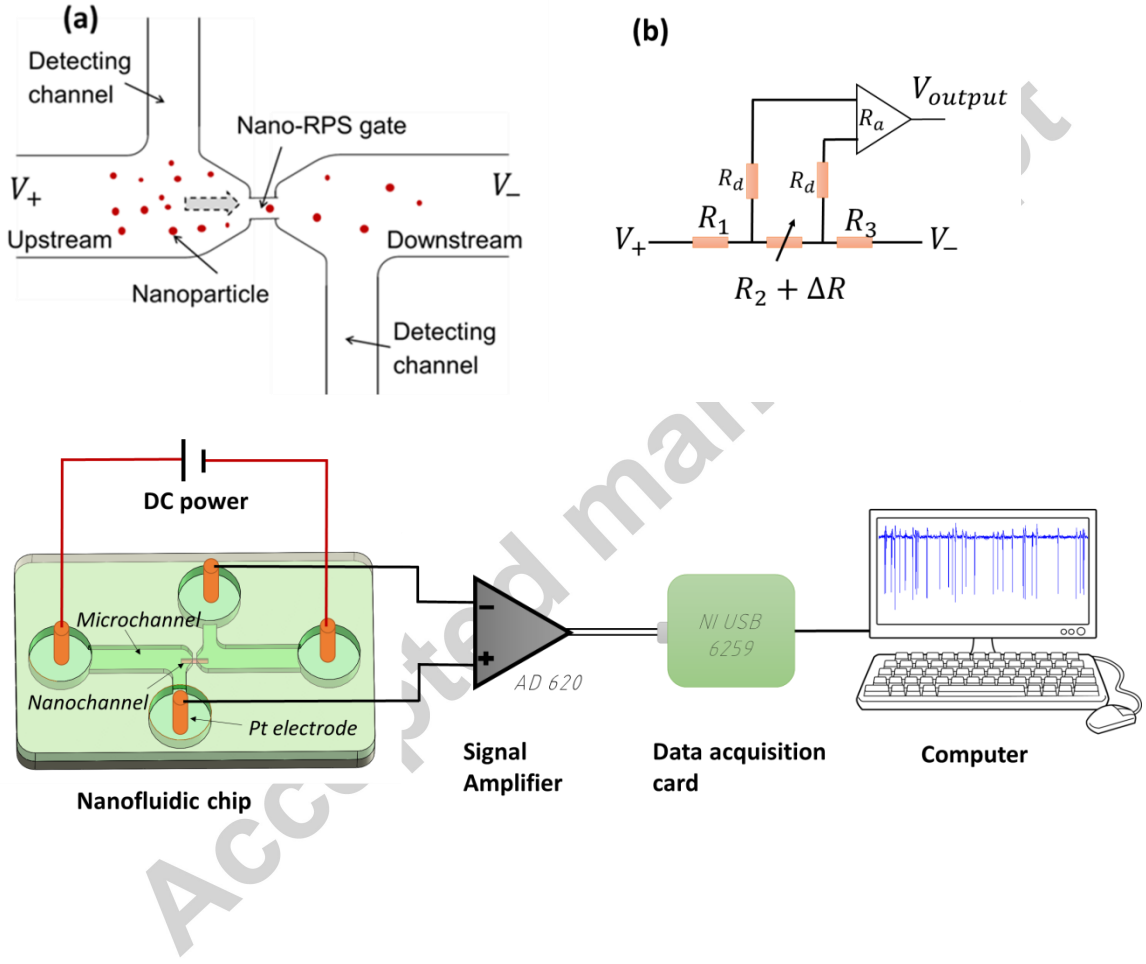

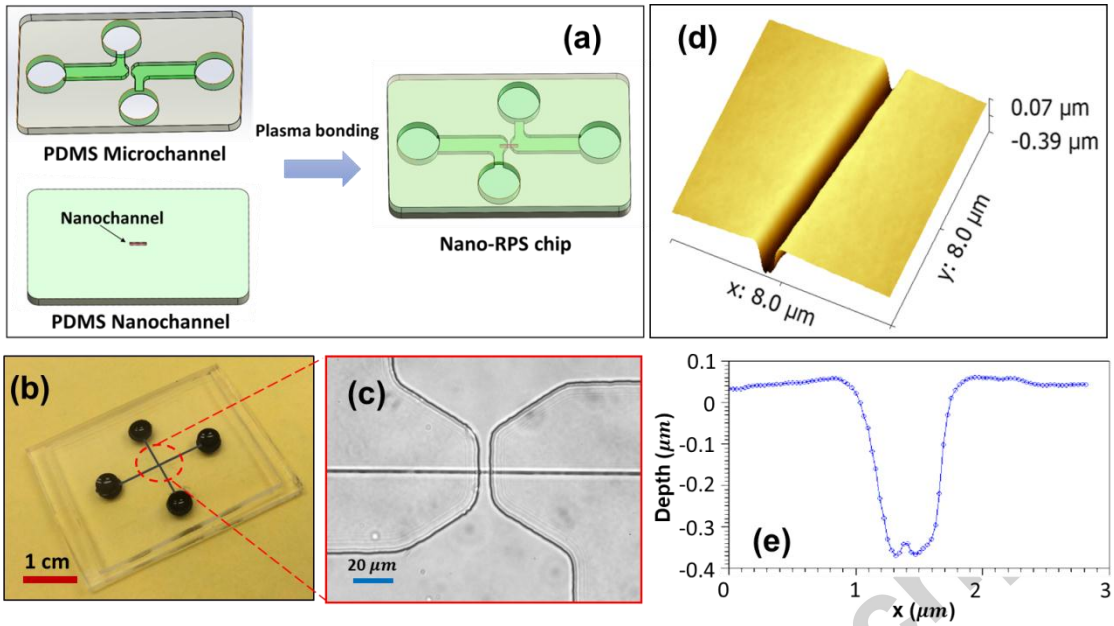
(a)
PDMS Microchannel
Plasma bonding
Nanochannel
PDMS Nanochannel
Nano-RPS chip
(d)
0.07 μm
-0.39 μm
x: 8.0 μm
y: 8.0 μm
(b)
1 cm
(c)
20 μm
(e)
Depth (μm)
x (μm)

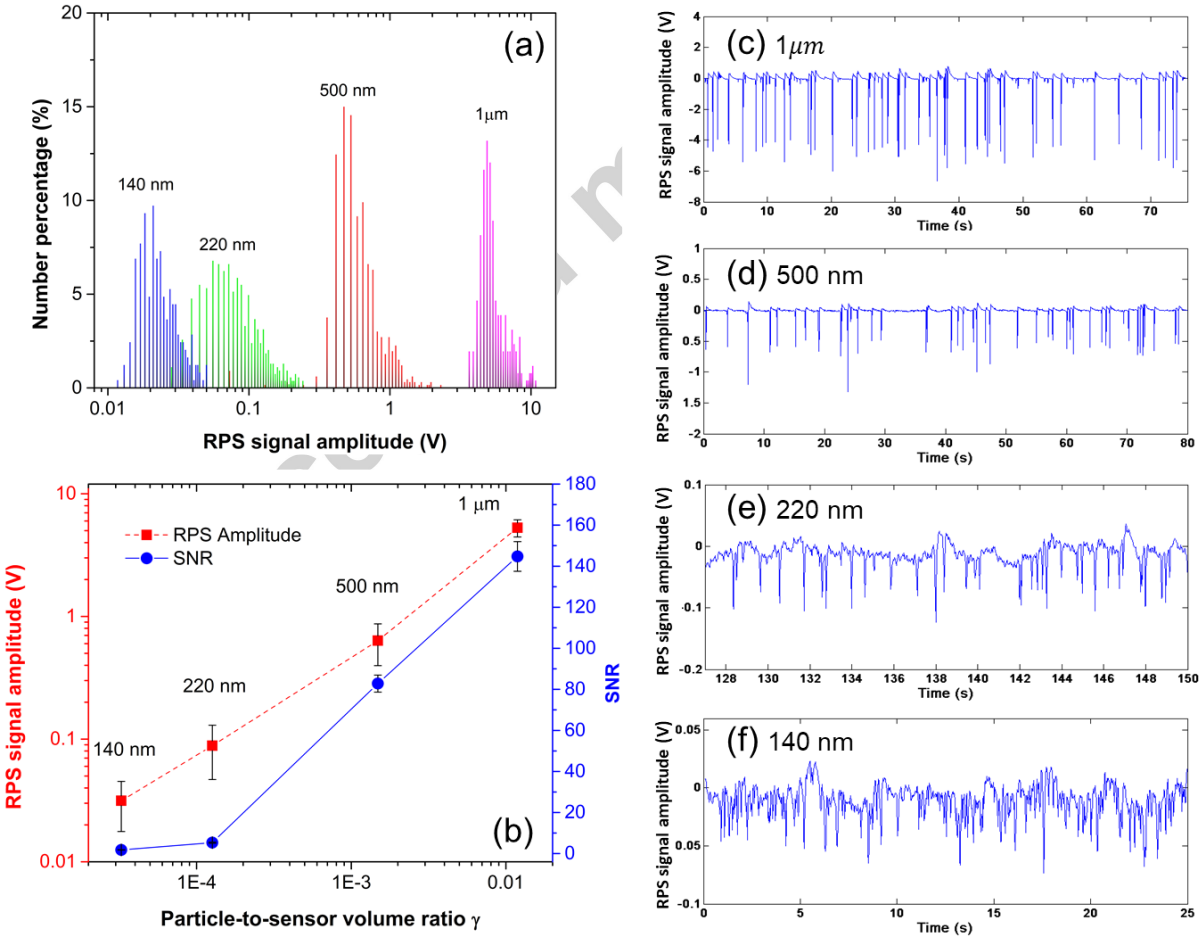
(a)
Number percentage (%)
140 nm
220 nm
500 nm
1μm
RPS signal amplitude (V)
(b)
RPS Amplitude
SNR
1 μm
500 nm
220 nm
140 nm
RPS signal amplitude (V)
SNR
Particle-to-sensor volume ratio γ
(c) 1μm
(d) 500 nm
(e) 220 nm
(f) 140 nm
RPS signal amplitude (V)
Time (s)

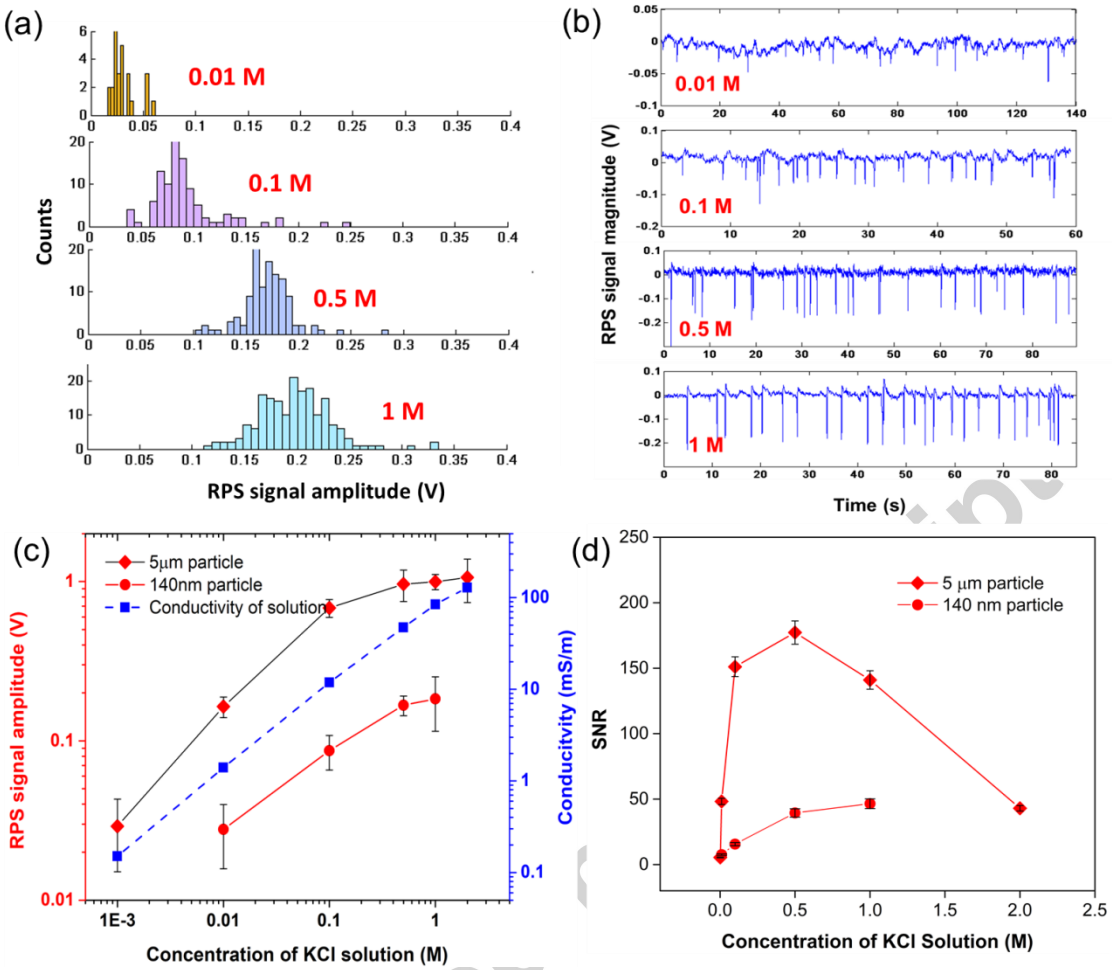

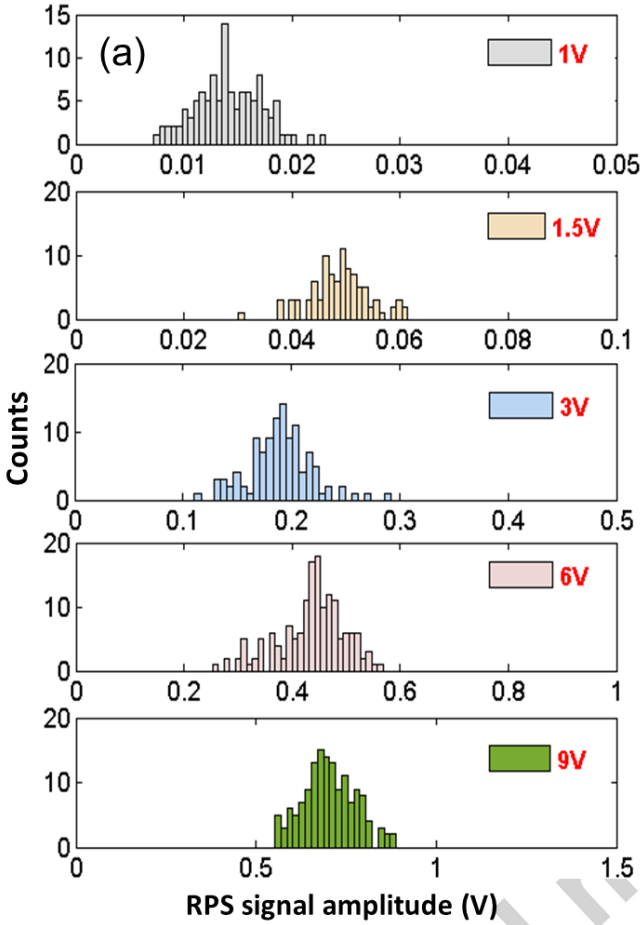
(a)
1V
1.5V
3V
6V
9V
Counts
RPS signal amplitude (V)

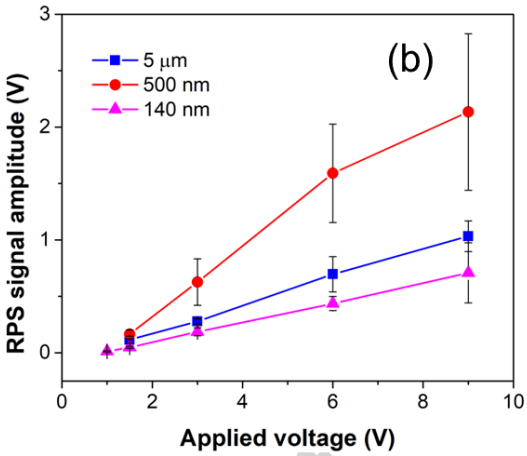
(b)
5 μm
500 nm
140 nm
RPS signal amplitude (V)
Applied voltage (V)

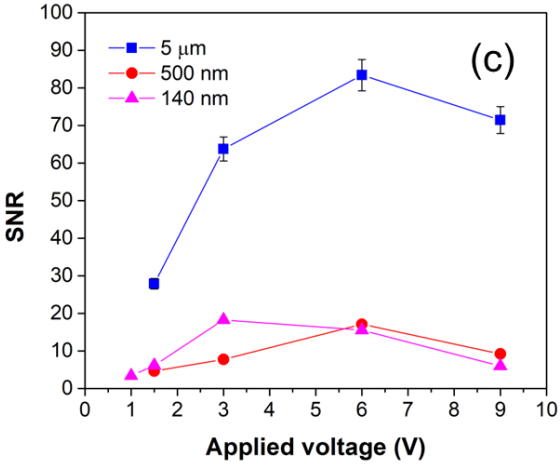
(c)
5 μm
500 nm
140 nm
SNR
Applied voltage (V)

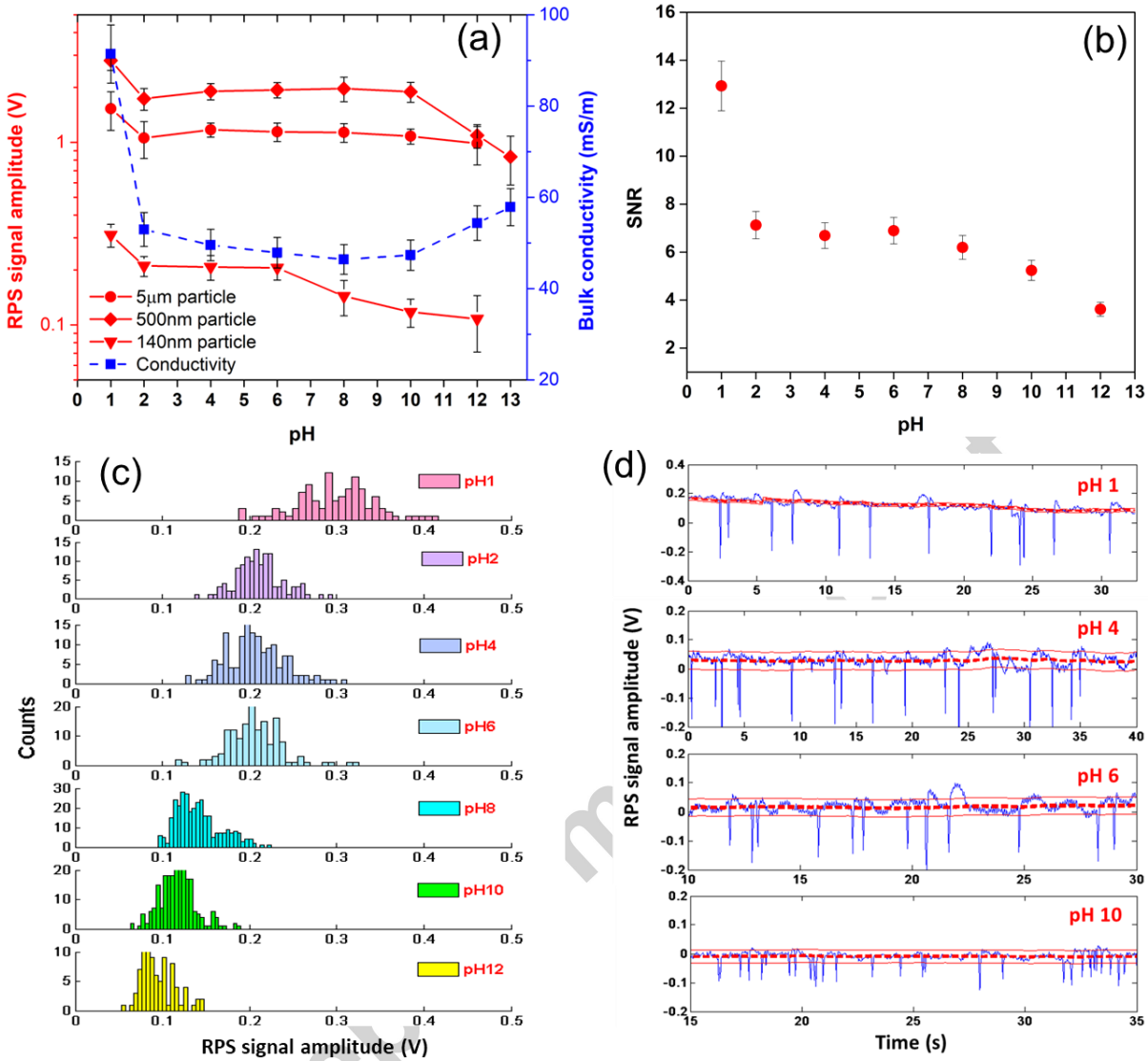

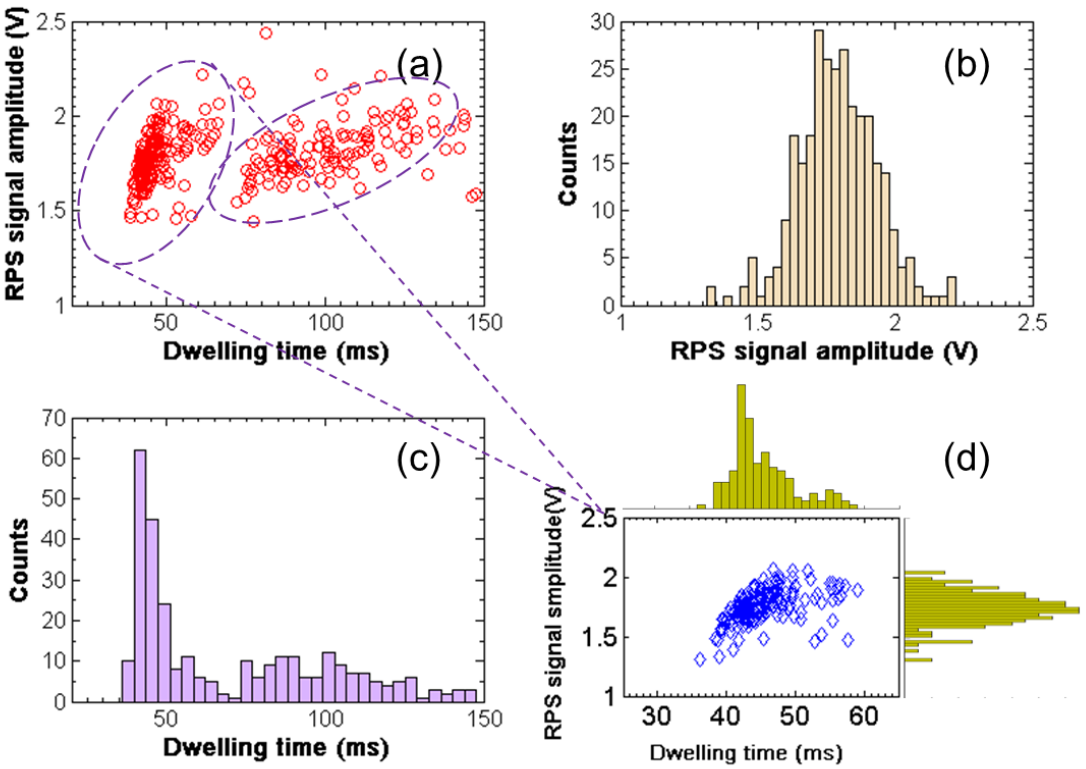

Graphical Abstract